Interlayer donor-acceptor pair excitons in MoSe₂/WSe₂ moiré heterobilayer

Hongbing Cai[1,2], Abdullah Rasmita[1], Qinghai Tan[1], Jia-Min Lai[3], Ruihua He[4], Disheng Chen[1,2], Naizhou Wang[1], Zhao Mu[1], Zumeng Huang[1], Zhaowei Zhang[1], John J. H. Eng[1,5], Yuanda Liu[1,2], Yongzhi She[6], Nan Pan[6], Xiaoping Wang[6], Xiaogang Liu[4], Jun Zhang[3] ✉, Weibo Gao[1,2,7] ✉

[1]*Division of Physics and Applied Physics, School of Physical and Mathematical Sciences, Nanyang Technological University, Singapore 637371, Singapore.*

[2]*The Photonics Institute and Centre for Disruptive Photonic Technologies, Nanyang Technological University, Singapore 637371, Singapore*

[3]*State Key Laboratory of Superlattices and Microstructures, Institute of Semiconductors, Chinese Academy of Sciences, Beijing 100083, China; Center of Materials Science and Optoelectronics Engineering, University of Chinese Academy of Sciences, Beijing 100049, China*

[4]*Department of Chemistry, National University of Singapore, Singapore 117543, Singapore.*

[5]*Institute of Materials Research and Engineering, Agency for Science, Technology and Research, Singapore, Singapore*

[6]*Department of Physics, University of Science and Technology of China, Hefei Anhui 230026, China.*

[7]*Centre for Quantum Technologies, National University of Singapore, Singapore.*

✉*e-mail: zhangjwill@semi.ac.cn; wbgao@ntu.edu.sg*

Localized interlayer excitons (LIXs) in two-dimensional moiré superlattices exhibit sharp and dense emission peaks, making them promising as highly tunable single-photon sources. However, the fundamental nature of these LIXs is still elusive. Here, we show the donor-acceptor pair (DAP) mechanism as one of the origins of these excitonic peaks. Numerical simulation results of the DAP model agree with the experimental photoluminescence spectra of LIX in the moiré MoSe₂/WSe₂ heterobilayer. In particular, we find that the emission energy-lifetime correlation and the nonmonotonic power dependence of the lifetime agree well with the DAP IX model. Our results provide insight into the physical mechanism of LIX formation in moiré heterostructures and pave new directions for engineering interlayer exciton properties in moiré superlattices.

The 2D transition metal dichalcogenide (TMD) bilayer is a promising platform for the study of strongly correlated electronic phenomena[1-7] and quantum optoelectronics applications. The moiré superlattice, which arises from the difference in lattice constant or a nonzero twist angle[8-10], can increase electron-electron interactions[11,12]. It also affects composite quasiparticles such as excitons (i.e., electron-hole pairs) [13-20], including interlayer excitons (IXs), where the electron and hole reside in different layers. The superlattice potential landscape confines IX in real space, resulting in a localized IX (LIX) with brightness that can be enhanced by placing the heterostructure on nanopillars[21]. Due to the localization effect and electron-exciton interaction, LIX is an excellent sensor for detecting strong electron-electron interactions[22-25]. Moreover, considering its large binding energy and nonzero out-of-plane electrical dipole[26,27], LIX could be used for electrically tunable quantum emitter arrays[28] operating at elevated temperatures.

One of the puzzling aspects of LIX emission in TMD moiré heterobilayers is the sharp and dense peaks observed in its photoluminescence (PL) spectrum[20,21,28-31]. While magneto-optical spectroscopy measurements have shown that these peaks are related to band-edge excitonic states[20,28,29], the number of these states predicted from theoretical calculations is only 10 states[14,18] or up to 20 states if the triplet IX state brightening[32] is considered. This number is much smaller than the number of observed peaks (more than 50), indicating other possible mechanisms[33]. It is urgent to uncover this mechanism as it is the key component for correlated phase manipulation and single photon emitter engineering.

Here, by analyzing the spectra and lifetimes of LIXs, we show that most of the LIX peaks in molybdenum diselenide (MoSe₂)/tungsten diselenide (WSe₂) heterobilayer on nanopillars come from donor-acceptor pair (DAP) exciton recombination. The DAP exciton[34-37] is a bound pair of an electron trapped in the donor site and a hole trapped in the acceptor site with a narrow linewidth PL emission due to its localization (see Fig. 1a). Its emission energy depends on the donor-acceptor distance[34], resulting in multiple sharp PL peaks. The interlayer DAP exciton (DAP IX) emission can account for more than 75% of the experimentally observed peak positions. Similar to the emission of localized defect exciton in TMD monolayer[38,39], the IX potential landscape created by the nanopillar-induced strain increases the coupling between the band-edge IX and localized DAP IX, enhancing the DAP IX emission (see Fig. 1b). By considering this coupling and the DAP exciton energy-lifetime relationship (i.e., lower energy DAP exciton has a longer lifetime[40]), we construct a DAP IX dynamic model, which fits well with the experimentally observed

LIX energy-lifetime correlation. Additionally, we have experimentally observed a unique nonmonotonic power dependence of the energy-resolved lifetime, which agrees well with the DAP IX dynamic model. The agreement between the experimental and theoretical results is strong evidence that the DAP IX is the primary origin of multiple sharp PL peaks in moiré heterobilayers. Our results reveal a novel physical mechanism behind LIX emission and open a new strategy for LIX emission modulation.
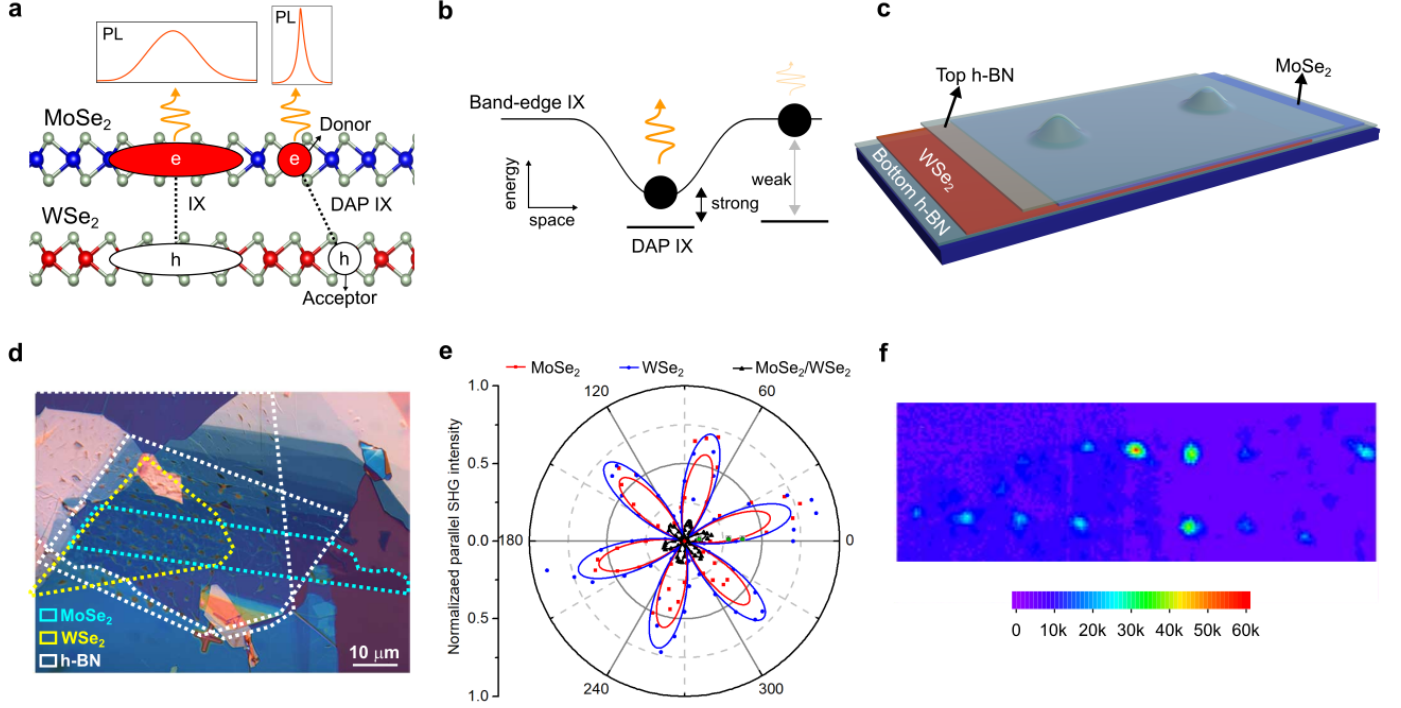

Fig. 1 | Device structure and LIX emission. a, Illustration of DAP IX. Localized DAP IX has a sharper emission than unlocalized IX. **b,** Enhancement of DAP IX emission by nanopillar. The strain-induced IX PL potential landscape enhances the coupling between band-edge IX and DAP IX, brightening the DAP IX emission. **c,** Sample structure. The sample consists of an hBN-encapsulated $MoSe_2/WSe_2$ on nanopillars. **d,** Optical microscopy image of the heterostructures fabricated by the all-dry transfer stacking method. **e,** Angle-dependent SHG intensity. The SHG shows that the twist angle is $\sim 60 \pm 1^{\circ}$. **f,** IX PL intensity map at 4.2 K under 765 nm (1.62 eV) laser excitation with an 850 long pass filter on the collection arm. Significant IX PL enhancement is observed at nanopillars, indicating LIX emission.

The sample structure used for the experiment is shown in Fig. 1c, and the optical microscope image of the sample is shown in Fig. 1d (see Extended Data Fig. 1(a, b) for the scanning electron microscope (SEM) image and see Methods for more details on the fabrication procedure). It consists of an hBN-encapsulated $MoSe_2/WSe_2$ heterostructure on a nanopillar array. Based on the second harmonic generation (SHG, Fig. 1e), the twist angle between the layers is close to $60 \pm 1^{\circ}$, i.e., an AB-stacking configuration[41]. This assignment of stacking configuration is also consistent with the g-factor measurement of the IX PL emission, showing a g-factor close to 16, expected for IX in AB stacked $MoSe_2/WSe_2$[20,42] (see Extended Data Fig. 2). As shown in Fig. 1f, the IX PL intensity map shows a significantly larger intensity for excitation at the nanopillar location than in the flat region, indicating that the LIX emission dominates the IX PL emission.

We next measured PL spectrum from the nanopillar locations. As shown in Fig. 2(a-c), the LIX PL emission consists of sharp and dense peaks, with the linewidth in the order of 100 μeV (see Extended Data Fig. 3 for PL peaks Lorentzian fitting), in contrast with the broad PL spectrum of the WSe_2 and $MoSe_2$ intralayer exciton on a flat monolayer (Extended Data Fig. 4). The LIX peaks have energy close to the band-edge IX central energies (around 1.4 eV for unstrained AB-stacked $MoSe_2/WSe_2$[42,43]). PL spectra from other nanopillar locations also show the same behaviour (see Extended Data Fig. 5). We then extract the peak position and compare them with the peak position predicted by the DAP model, which can be approximated as [34]

$$E(R_m) = E_0 + \frac{\alpha}{R_m}, \tag{1}$$

where E_0 is the minimum DAP IX energy, R_m is the mth distance between the donor and acceptor (with integer m being the shell number), and $\alpha = \frac{e^2}{4\pi\varepsilon}$ where e is the electron charge and ε is the effective permittivity. The possible R_m values are determined

2

by the lattice constant and interlayer distance (see Fig. 2d for an illustration of R_1 and R_2). The predicted DAP IX peak positions are shown as red lines in Fig. 2(a-c) and plotted together with the experimentally obtained peak positions in Figs. 2(e-g). More than 75% of the observed peaks match the predicted DAP IX peaks (Fig. 2h), indicating a good agreement between the DAP model and experimental results (see Supplementary Information Section 1 for more details on the PL peak analysis).
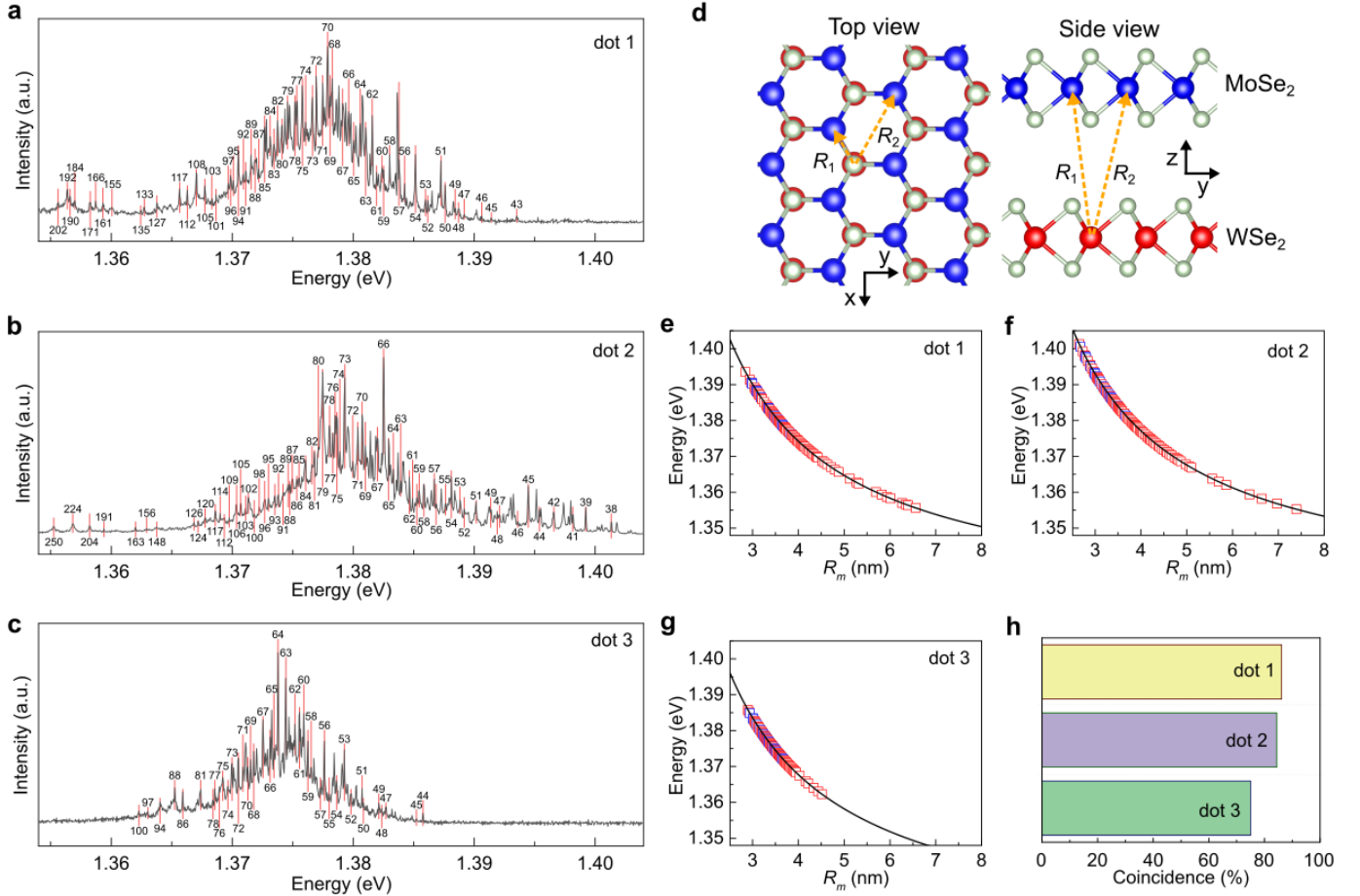

Fig. 2 | **DAP IX PL spectra. a-c,** IX PL spectra. Solid black lines are the measured spectra. Red dash lines are the predicted DAP IX peaks, with the labels indicating the shell numbers. **d,** Illustration of DAP IX in the van der Waals heterobilayer. R_1 and R_2 are the first two smallest distances between the donor-acceptor pair. **e-g,** Calculated DAP IX peak positions (lines) vs. experimentally obtained peak positions (symbols). The red (blue) symbols are the peak positions that (do not) match the DAP IX peak positions. **h,** DAP model goodness of fit. The coincidence, defined as the number of experimentally observed peaks matching the DAP IX peaks divided by the total number of experimentally observed peaks, represents the goodness of fit.

We found that the maximum donor-acceptor distance is ~8 nm, which agrees with the DAP IX model. In particular, due to the deep moiré superlattice potential in slightly twisted MoSe$_2$/WSe$_2$ [44], it is unlikely that the donor and acceptor are located at two different moiré sites. Hence, the maximum donor-acceptor distance must be less than the moiré period. In our case of $60 \pm 1°$ twisted MoSe$_2$/WSe$_2$, the moiré period is ~20 nm[17], which is significantly larger than the maximum-donor acceptor distance, indicating the adequacy of the DAP IX model.

Further evidence for the DAP model is obtained from energy- and time-resolved PL measurements of the LIXs. The IX PL spectrum time trace under pulsed 726-nm diode laser excitation shows no jittering behaviour (Fig. 3a), allowing a reliable time-resolved PL measurement of an emission peak. A homemade spectrometer (Fig. 3b) was used to filter the emission of a chosen peak for the time-resolved PL measurement (see Extended Data Fig. 6 for filtered PL emission spectra). Typical time-resolved PL of different emission peaks are shown in Fig. 3c. The experimental data fit well with the double exponential decay function, indicating that at least two different states are involved. We attribute these two states to DAP IX and band-edge IX states.

The extracted decay rate constants are plotted in Fig. 3d. Instead of a monotonous change, fast (k_1) and slow (k_2) decay rates reach maximum values at particular energy values. This observation can be explained by considering the dynamics of DAP IX

and its coupling to the band-edge IX (see inset in Fig. 1d), where DAP IX decays faster than band-edge IX. For the case where $k_1 \gg k_2$, the decay rates can be approximated as

$$k_1 \approx k_{DAP} = k_{nr} + k_{r0} \exp\left(-\frac{2\alpha}{R_B(E-E_0)}\right), \tag{2}$$

$$k_2 \approx k_{IX} + D, \tag{3}$$

where k_{DAP} is the DAP IX total decay rate, k_{nr} is the DAP IX nonradiative decay rate, k_{r0} is the DAP IX maximum radiative decay rate, R_B is the donor (acceptor) Bohr radius (whichever is largest), k_{IX} is the band-edge IX decay rate, D is the coupling rate between the band-edge and DAP IX, and other parameters are the same as in Eq. (1). Considering the coupling between the DAP and band-edge IX, the values of R_B and D depend on the energy difference between these two IX states. The coupling rate between the DAP and band-edge IX is maximum when their energy is the same. Due to this coupling, the DAP IX state is a combination of the uncoupled DAP IX and band-edge IX states. Since the band-edge carrier has a larger Bohr radius than the donor (acceptor) one, the coupling also increases the value of DAP IX's R_B. Hence, both R_B and D reach maximum values for the peak energy equal to the band-edge IX central energy, which results in the maximum values for both fast and slow decay rates according to Eqs. (2) and (3). As shown in Fig. 3d, there is an excellent agreement between this model and the data, further confirming the DAP IX mechanism (see Supplementary Information Section 2 for more details on the calculation of DAP IX energy-lifetime correlation). Two band-edge IX peaks were detected (labelled as E_{IX1} and E_{IX2}), with ~7 meV peak separation. This peak separation value agrees with the IX trion binding energy in MoSe$_2$/WSe$_2$[23,45], indicating that these two peaks are neutral and charged band-edge IX peaks. Similar behaviour is also observed for other dots (see Fig. 3(e,f) for the results for dot 3).
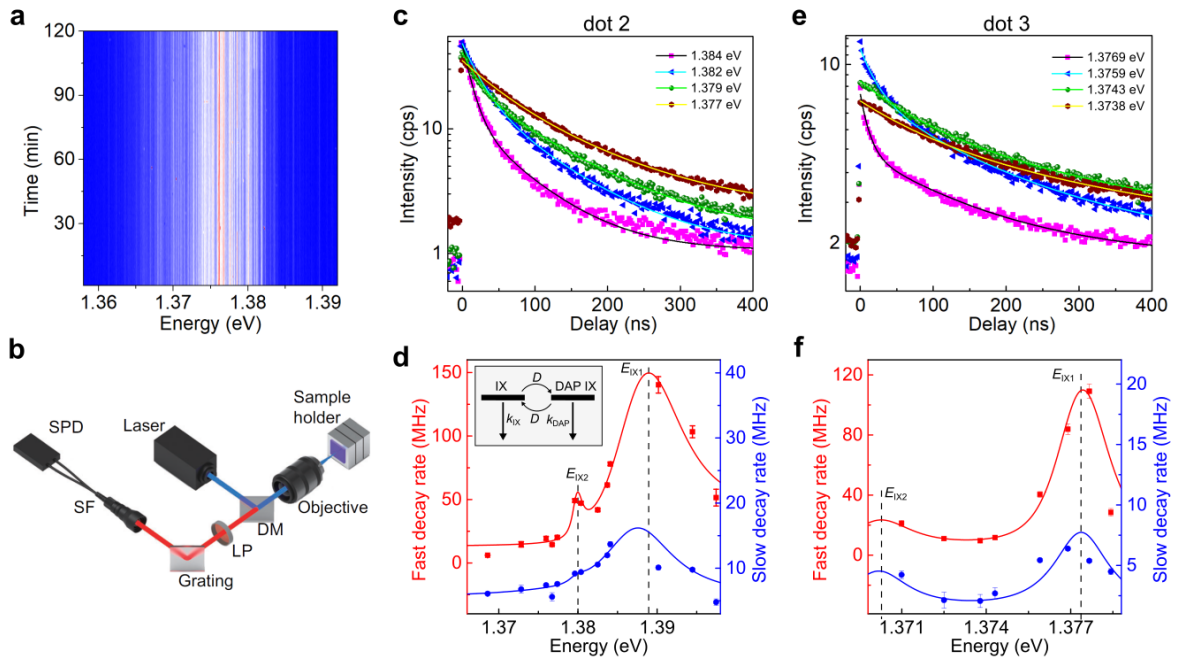

Fig. 3 | Lifetime-energy correlation of LIX emission. a, IX PL spectrum time trace. **b,** Experimental setup. A high transmittance grating was used to spatially separate emissions from different peaks. **c,** Energy- and time-resolved PL of LIX emission. Data (shown as symbols) was obtained with excitation location at dot 2 (as in Fig. 1c) under a 6 nW excitation. The lines are double exponential decay fitting results. **d,** Decay rates vs. emission energy for dot 2. The lines are the fitting results using the DAP IX dynamic model. The dashed lines mark the central energies of band-edge IXs used for the fitting. Inset: DAP-band edge IX coupling model. The downward straight arrows represent decay rates, while the curved arrows represent coupling rates. **e, f,** Like c and d but for dot 3 under a 2 nW excitation.

The dependence of the decay rate on the coupling between the DAP IX and band-edge IX suggests that the power dependence of the decay rates should also show a nonmonotonous trend. In general, IX decay rates increase with increasing power due to the increase in the nonradiative decay rate[46]. However, an increase in power also causes a power-induced blue shift in IX energy due to dipole-dipole repulsion[47,48], which can have different magnitudes for localized DAP IX and band-edge IX[31]. As illustrated in Fig. 4a, a DAP IX peak which is initially resonant with the band-edge IX at low power, becomes less resonant as power increases.

4

The increased energy gap between the band-edge and DAP IX results in the decoupling between the two IX states, reducing the Bohr radius. Consequently, the fast decay rate decreases when the power is increased (see Eq. (2)). Further increasing the power does not result in significant decoupling, and the usual power-induced increase in decay rate is observed. Hence, in addition to the general density-dependent increase, decay rates, especially the fast decay rate, should exhibit nonmonotonous energy-dependent change.
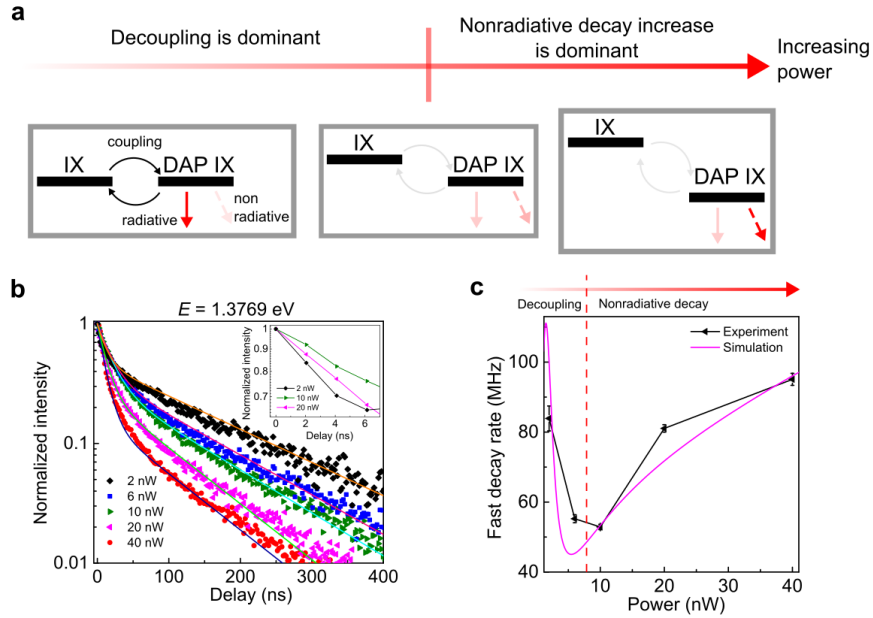

Fig. 4 | Power dependence of the LIX lifetime. a, Schematic of power-dependent decay rate mechanism. The downward straight arrows represent decay rates with solid (dashed) lines indicating (non)radiative decay rates, and darker colour means faster decay rates. The curved arrows represent coupling rates. With increasing power, the nonradiative rate increases. Additionally, the energy spacing of the DAP-band edge IX increases, reducing the coupling and narrowing the Bohr radius, resulting in a decrease in the DAP IX radiative decay rate. **b,** Normalized time-resolved photoluminescence of LIX with the same photon energy (1.3769 eV) under different laser powers. The data (shown as symbols) are obtained with the excitation location at dot 3 (as in Fig. 1c and Fig. 3(e,f)). The inset shows measured data for 2, 10, and 20 nW at the $0 - 7$ ns time range, exhibiting the nonmonotonous power dependence of the fast decay rate. The lines are the results of double exponential decay fitting. **c,** Experimental and simulated fast decay rate vs excitation power.

To verify this, we measured the power dependence of the energy- and time-resolved PL for power from 2 nW to 40 nW. Power-dependent PL spectra (Extended Data Fig. 7) can be fitted with multiple Lorentzians, indicating that the emission in this power range is still dominated by LIX emission. Individual peak positions do not show a power-dependent blueshift, agreeable with previous reports[31]. The measured power-dependent time-resolved PLs for the peak with an energy of 1.3769 eV are shown in Fig. 4b, together with the double exponential fitting. As predicted, the extracted fast (k_1) decay rate, shown in Fig. 4c, exhibits a nonmonotonous power dependence. We simulate power-dependent decay rates following the DAP IX dynamic model. Simulation results show similar trends to experimental results, supporting the DAP IX hypothesis. The simulated results for other peaks, including the fast and slow decay rates, are also consistent with the experimental result (see Extended Data Fig. 8 and Supplementary Information Section 3).

In summary, we have theoretically proposed and experimentally confirmed a novel DAP IX mechanism as the origin of the dense and sharp IX emissions from MoSe2/WSe2 on nanopillars. Our experimental results, including energy- and time-resolved PL measurements and the lifetime's power dependence, provide strong evidence for the DAP IX model. Our work renders novel insight into the nature of LIX emission in 2D heterostructures and highlights the interplay between the disorder (represented by the DAP IX) and superlattice potential (represented by the band-edge IX) in the correlated moiré material. Further development of our results includes the demonstration of an atomic position-controlled method to generate and manipulate interlayer exciton emission on-demand, which is crucial for quantum information and simulators[49] based on 2D semiconductors.

1   Xu, Y. *et al.* Correlated insulating states at fractional fillings of moiré superlattices. *Nature* **587**, 214-218 (2020).
2   Regan, E. C. *et al.* Mott and generalized Wigner crystal states in WSe2/WS2 moiré superlattices. *Nature* **579**, 359-363 (2020).
3   Tang, Y. *et al.* Simulation of Hubbard model physics in WSe2/WS2 moiré superlattices. *Nature* **579**, 353-358 (2020).

4   Wang, L. *et al.* Correlated electronic phases in twisted bilayer transition metal dichalcogenides. *Nat. Mater.* **19**, 861-866 (2020).

5   Chu, Z. *et al.* Nanoscale conductivity imaging of correlated electronic states in WSe₂/WS₂ moiré superlattices. *Phys. Rev. Lett.* **125**, 186803 (2020).

6   Huang, X. *et al.* Correlated insulating states at fractional fillings of the WS₂/WSe₂ moiré lattice. *Nat. Phys.* **17**, 715-719 (2021).

7   Li, T. *et al.* Quantum anomalous Hall effect from intertwined moiré bands. *Nature* **600**, 641-646 (2021).

8   van der Zande, A. M. *et al.* Tailoring the electronic structure in bilayer molybdenum disulfide via interlayer twist. *Nano Lett.* **14**, 3869-3875 (2014).

9   Zhang, C. *et al.* Interlayer couplings, moiré patterns, and 2D electronic superlattices in MoS₂/WSe₂ hetero-bilayers. *Sci. Adv.* **3**, e1601459 (2017).

10   Pan, Y. *et al.* Quantum-confined electronic states arising from the moiré pattern of MoS₂–WSe₂ heterobilayers. *Nano Lett.* **18**, 1849-1855 (2018).

11   Suárez Morell, E., Correa, J. D., Vargas, P., Pacheco, M. & Barticevic, Z. Flat bands in slightly twisted bilayer graphene: Tight-binding calculations. *Phys. Rev. B* **82**, 121407 (2010).

12   Bistritzer, R. & MacDonald, A. H. Moiré bands in twisted double-layer graphene. *Proc. Natl. Acad. Sci. U. S. A.* **108**, 12233-12237 (2011).

13   Wu, F., Lovorn, T. & MacDonald, A. H. Topological exciton bands in moiré heterojunctions. *Phys. Rev. Lett.* **118**, 147401 (2017).

14   Brem, S., Linderälv, C., Erhart, P. & Malic, E. Tunable phases of moiré excitons in van der Waals heterostructures. *Nano Lett.* **20**, 8534-8540 (2020).

15   Jin, C. *et al.* Observation of moiré excitons in WSe₂/WS₂ heterostructure superlattices. *Nature* **567**, 76-80 (2019).

16   Alexeev, E. M. *et al.* Resonantly hybridized excitons in moiré superlattices in van der Waals heterostructures. *Nature* **567**, 81-86 (2019).

17   Tran, K. *et al.* Evidence for moiré excitons in van der Waals heterostructures. *Nature* **567**, 71-75 (2019).

18   Wu, F., Lovorn, T. & MacDonald, A. H. Theory of optical absorption by interlayer excitons in transition metal dichalcogenide heterobilayers. *Phys. Rev. B* **97**, 035306 (2018).

19   Yu, H., Liu, G.-B., Tang, J., Xu, X. & Yao, W. Moiré excitons: From programmable quantum emitter arrays to spin-orbit-coupled artificial lattices. *Sci. Adv.* **3**, e1701696 (2017).

20   Seyler, K. L. *et al.* Signatures of moiré-trapped valley excitons in MoSe₂/WSe₂ heterobilayers. *Nature* **567**, 66-70 (2019).

21   Montblanch, A. R. P. *et al.* Confinement of long-lived interlayer excitons in WS₂/WSe₂ heterostructures. *Commun. Phys.* **4**, 119 (2021).

22   Baek, H. *et al.* Optical read-out of Coulomb staircases in a moiré superlattice via trapped interlayer trions. *Nat. Nanotechnol.* **16**, 1237-1243 (2021).

23   Liu, E. *et al.* Signatures of moiré trions in WSe₂/MoSe₂ heterobilayers. *Nature* **594**, 46-50 (2021).

24   Miao, S. *et al.* Strong interaction between interlayer excitons and correlated electrons in WSe₂/WS₂ moiré superlattice. *Nat. Commun.* **12**, 3608 (2021).

25   Liu, E. *et al.* Excitonic and valley-polarization signatures of fractional correlated electronic phases in a WSe₂/WS₂ moiré superlattice. *Phys. Rev. Lett.* **127**, 037402 (2021).

26   Rivera, P. *et al.* Observation of long-lived interlayer excitons in monolayer MoSe₂–WSe₂ heterostructures. *Nat. Commun.* **6**, 6242 (2015).

27   Jauregui, L. A. *et al.* Electrical control of interlayer exciton dynamics in atomically thin heterostructures. *Science* **366**, 870-875 (2019).

28   Baek, H. *et al.* Highly energy-tunable quantum light from moiré-trapped excitons. *Sci. Adv.* **6**, eaba8526 (2020).

29   Brotons-Gisbert, M. *et al.* Spin–layer locking of interlayer excitons trapped in moiré potentials. *Nat. Mater.* **19**, 630-636 (2020).

30   Brotons-Gisbert, M. *et al.* Moiré-trapped interlayer trions in a charge-tunable WSe₂/MoSe₂ heterobilayer. *Phys. Rev. X* **11**, 031033 (2021).

31   Kremser, M. *et al.* Discrete interactions between a few interlayer excitons trapped at a MoSe₂–WSe₂ heterointerface. *npj 2D Mater. Appl.* **4**, 8 (2020).

32   Yu, H., Liu, G.-B. & Yao, W. Brightened spin-triplet interlayer excitons and optical selection rules in van der Waals heterobilayers. *2D Mater.* **5**, 035021 (2018).

33   Mahdikhanysarvejahany, F. *et al.* Localized interlayer excitons in MoSe₂–WSe₂ heterostructures without a moiré potential. *Nat. Commun.* **13**, 5354 (2022).

34   Hopfield, J. J., Thomas, D. G. & Gershenzon, M. Pair spectra in GaP. *Phys. Rev. Lett.* **10**, 162-164 (1963).

35   Dischler, B. *et al.* Resolved donor-acceptor pair-recombination lines in diamond luminescence. *Phys. Rev. B* **49**, 1685-1689 (1994).

36   Choyke, W. J. & Patrick, L. Luminescence of donor-acceptor pairs in cubic SiC. *Phys. Rev. B* **2**, 4959-4965 (1970).

37   Tan, Q. *et al.* Donor–acceptor pair quantum emitters in hexagonal boron nitride. *Nano Lett.* **22**, 1331-1337 (2022).

38   Linhart, L. *et al.* Localized intervalley defect excitons as single-photon emitters in WSe₂. *Phys. Rev. Lett.* **123**, 146401 (2019).

39   Parto, K., Azzam, S. I., Banerjee, K. & Moody, G. Defect and strain engineering of monolayer WSe₂ enables site-controlled single-photon emission up to 150 K. *Nat. Commun.* **12**, 3585 (2021).

40   Thomas, D. G., Hopfield, J. J. & Augustyniak, W. M. Kinetics of radiative recombination at randomly distributed donors and acceptors. *Phys. Rev.* **140**, A202-A220 (1965).

41   Hsu, W.-T. *et al.* Second harmonic generation from artificially stacked transition metal dichalcogenide twisted bilayers. *ACS Nano* **8**, 2951-2958 (2014).

42   Nagler, P. *et al.* Giant magnetic splitting inducing near-unity valley polarization in van der Waals heterostructures. *Nat. Commun.* **8**, 1551 (2017).

43   Wang, T. *et al.* Giant valley-Zeeman splitting from spin-singlet and spin-triplet interlayer excitons in WSe₂/MoSe₂ heterostructure. *Nano Lett.* **20**, 694-700 (2020).

44   Shabani, S. *et al.* Deep moiré potentials in twisted transition metal dichalcogenide bilayers. *Nat. Phys.* **17**, 720-725 (2021).

45   Wang, X. *et al.* Moiré trions in MoSe₂/WSe₂ heterobilayers. *Nat. Nanotechnol.* **16**, 1208-1213 (2021).

46   Wang, J. *et al.* Optical generation of high carrier densities in 2D semiconductor heterobilayers. *Sci. Adv.* **5**, eaax0145 (2019).

47   Nagler, P. *et al.* Interlayer exciton dynamics in a dichalcogenide monolayer heterostructure. *2D Mater.* **4**, 025112 (2017).

48 Li, W., Lu, X., Dubey, S., Devenica, L. & Srivastava, A. Dipolar interactions between localized interlayer excitons in van der Waals heterostructures. *Nat. Mater.* **19**, 624-629 (2020).

49 Kennes, D. M. *et al.* Moiré heterostructures as a condensed-matter quantum simulator. *Nat. Phys.* **17**, 155-163 (2021).

Methods

Sample fabrications. A standard electron beam lithography (EBL) process was carried out on an FEI system (Helios 600 NanoLab, FEI) to fabricate the nanopillars. Negative e-beam HSQ (6%) resist was spin-coated on a Si/SiO$_2$ substrate at 4000 rpm to form a 150 nm thick resist film and baked on a hotplate at 150 °C for 5 min. The electron high tension (EHT) of the EBL system was set to be 30 kV with a beam current of 30 pA. The line dose used was 1.2 μC/cm. A 1 % NaOH solution was used as the developer, and DI water was used as the stopper. Nanopillars fabricated on a Si/SiO$_2$ substrate have diameters ranging from 100 to 300 nm, and a height of 130 nm (see Extended Data Fig. 1).

WSe$_2$ and MoSe$_2$ monolayers were mechanically exfoliated from bulk materials (2D Semi) and transferred onto SiO$_2$ nanopillars using a standard method. The WSe$_2$ and MoSe$_2$ monolayers were first prepared and characterized on PDMS and then transferred onto the nanopillar array using the transfer stage (Meta Inc.) with an alignment resolution of less than 1 μm and an angle controllability of smaller than 1°. The heterostructures were encapsulated between two thin layers of h-BN with a thickness of several nanometers. The whole sample was then annealed in a high vacuum (10^{-7} mBar) at 200 °C for 2 hours.

Photoluminescence spectroscopy. Low-temperature (4.2 K) photoluminescence spectroscopy was carried out in home-built spectroscopy setups loaded into a cryostat. (AttoDry 1000). All low-temperature PL spectra were obtained using a 100× objective (NA=0.8) with a spot size of about 500 nm in the cryostat at 4 K. PL spectra were collected with a high-resolution spectrometer (Princeton Instrument, PyLoN CCD). The gratings used in the spectrometers were 300 g/mm and 1200 g/mm, both blazed at 750 nm. The excitation laser was an energy-tunable continuous-wave laser (M squared) coupled to a single-mode fibre. For lifetime experiments, a pulsed 726-nm diode laser (maximum repetition rate of 80 MHz with a full width at half maximum of <80 ps) was used to excite the sample. The intensity map was obtained by detecting the emission using a superconducting single-photon detector (Gifford-McMahon cycle SSPD from SCONTEL) while scanning the sample using a pair of high-resolution stages (ANSx150/LT). To filter the single sharp peak from the dense and discrete emission lines, high transparency gratings (IBSNE Photonics, FSTG-SNIR966-915) were used after the PL collection side from the sample and then sent to the spectrometer or avalanche photodiodes (APDs). A time-correlated photon counting card (Picoharp, PH300) was used to obtain the time-resolved PL data.
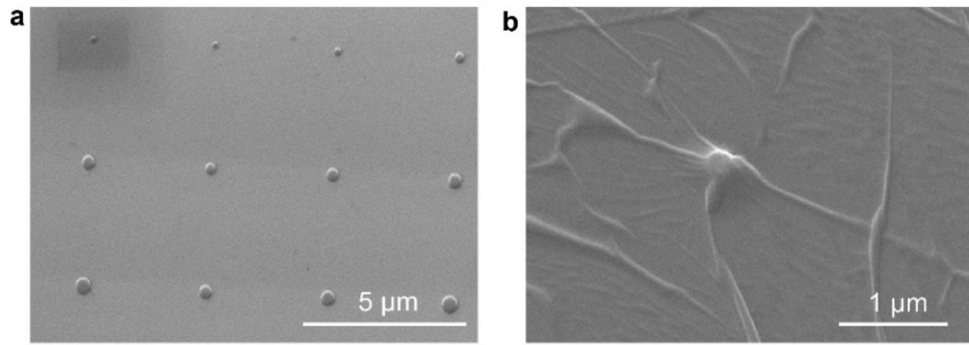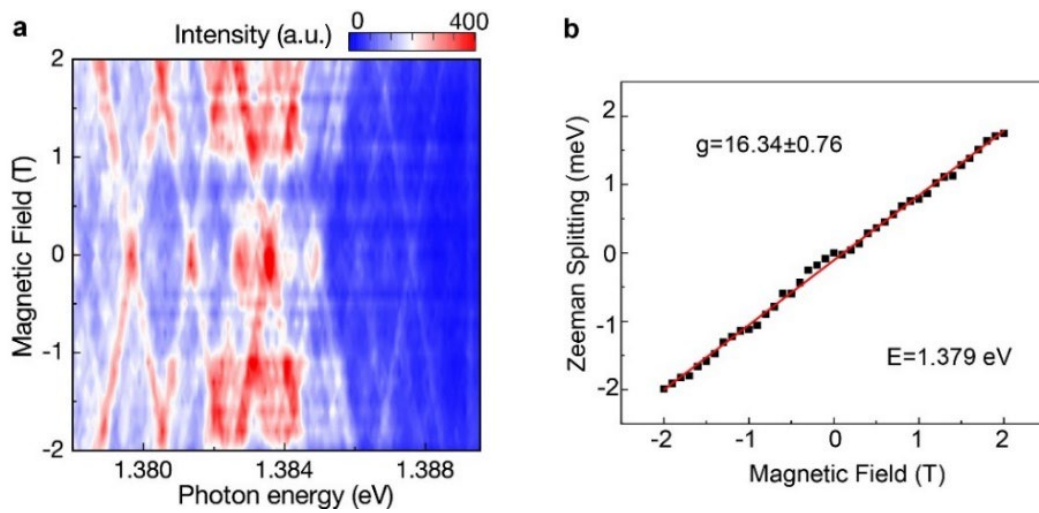
**Extended Data Fig. 1 | SEM image of the sample. a, b** SEM image of the sample showing the nanopillar array and the heterostructure laid on top of it.


Extended Data Fig. 2 | Magnetic field dependence of LIX PL spectrum. a, LIX PL spectrum as a function of the applied out-of-plane magnetic fields at 4.2 K under 765 nm (1.62 eV) laser excitation. Circular polarization filters were not used in the collection and excitation part. An 850 nm long pass filter is used in the collection arm. **b,** Magnetic field dependence of the Zeeman splitting for one of the LIX peaks (with emission energy of 1.379 eV @ 0 T peak). The linear fitting shows an effective g-factors of 16.34±0.76.
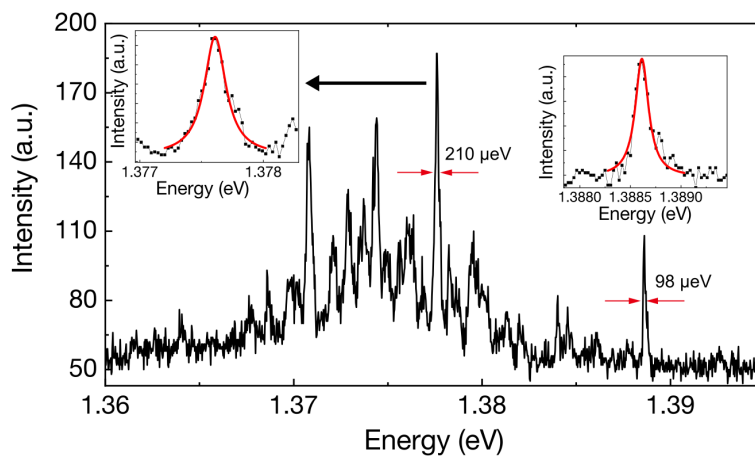

Extended Data Fig. 3 | Typical linewidths of LIX peaks. Lorentzian fittings of LIX peaks show FWHM of 210 μeV (for the 1.377 eV peak) and 98 μeV (for the 1.389 eV peak). The experimental condition is the same as in Extended Data Fig. 2.
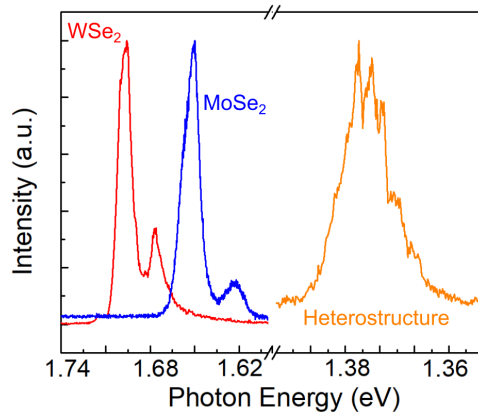
Extended Data Fig. 4 | Typical PL spectrum under a 532 nm laser excitation at flat monolayer MoSe₂, flat monolayer WSe₂, and the heterobilayer on nanopillar area.
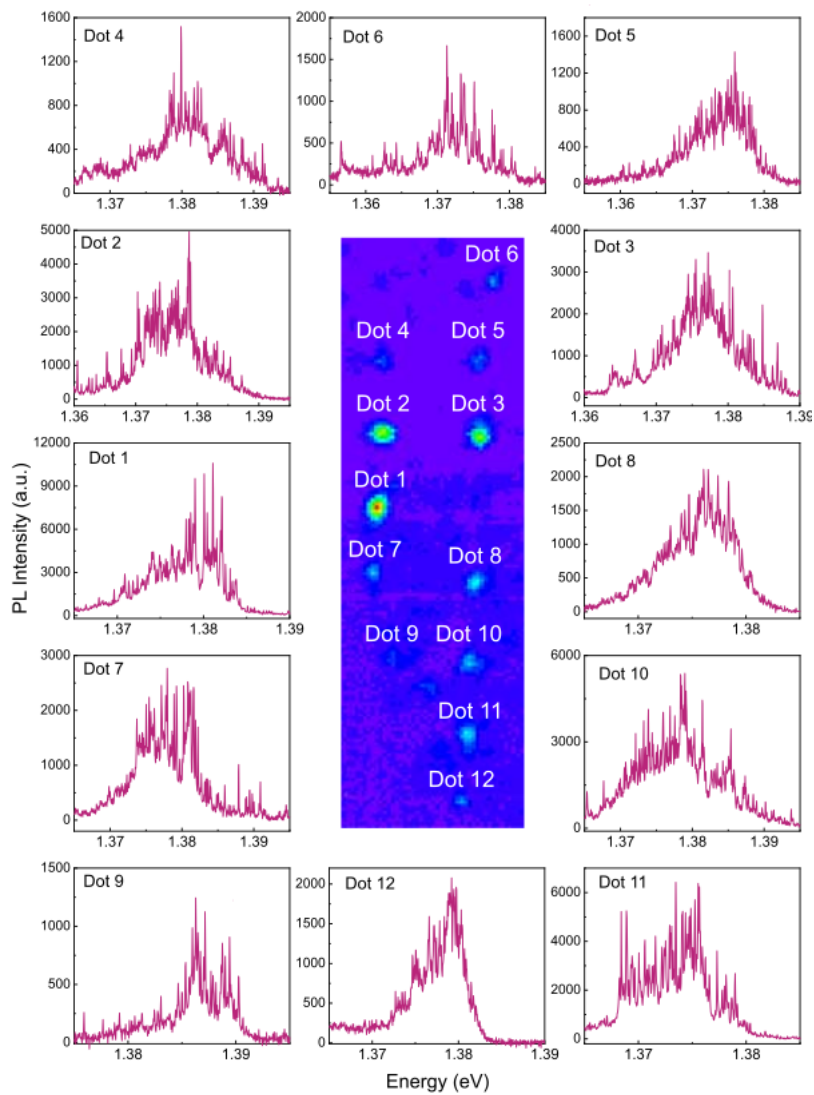
**Extended Data Fig. 5 | LIX PL spectra from various nanopillars.** Middle: PL intensity map. The IX PL intensity map shows a significant intensity enhancement at nanopillars. Around: PL spectra at various excitation locations (labelled as Dot 1 to Dot 12 on the map). The IX PL spectra show multi peaks with the FWHMs ranging from 100 to 800 μeV. The experimental condition is the same as in Extended Data Fig. 2.
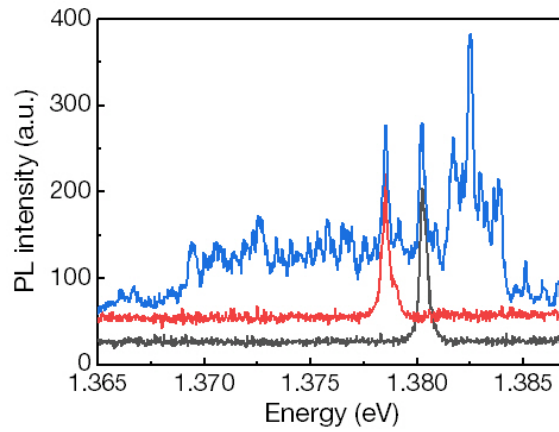
Extended Data Fig. 6 | Grating-filtered LIX PL spectrum. The blue line is the IX PL before the filtering by the grating. Two typical LIX PLs after filtering are shown as red and black lines, showing an FWHM of around 700 µeV.
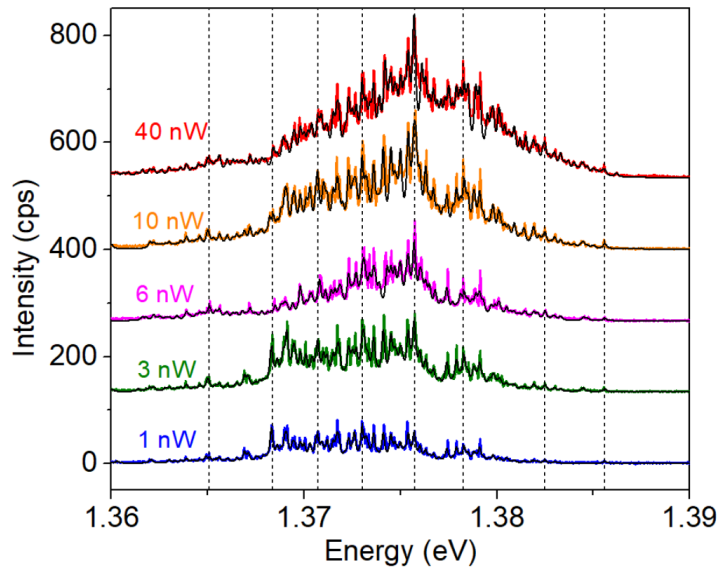
Extended Data Fig. 7 | Lorentzian fitting of IX emission at various powers. Solid black lines are multiple Lorentzian fittings. The dashed lines indicate the tracking of some peaks. There is no clear power-dependent blue shift observed.
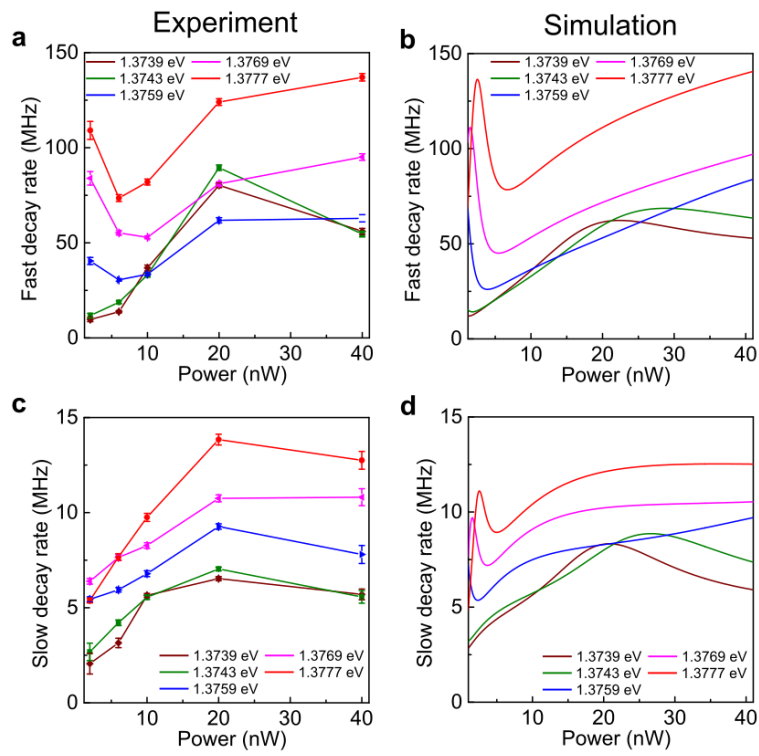
Extended Data Fig. 8 | Power dependence of decay rates. a, Experimental and **b,** simulated fast decay rates vs excitation power. **c,** Experimental and **d,** simulated slow decay rates vs excitation power.

Supplementary information:

Interlayer donor-acceptor pair excitons in MoSe₂/WSe₂ moiré heterobilayer

<u>Section 1. PL spectrum peak analysis</u>

This section discusses how we estimate the band-edge IX and DAP IX peak positions. We first discuss the band-edge IX peak determination. Using the band-edge IX peak energy and considering the DAP IX peak linewidth, we then determine the minimum energy of DAP IX. Finally, we discuss how we use the DAP peak formula to obtain the predicted DAP IX peaks.

For the band-edge IX, considering the coupling between band-edge and DAP IXs, its peak energy (E_{IX}) should be close to the dominant DAP IX peak (i.e., the IX energy with the brightest PL emission). Additionally, due to the non-uniform energy distribution of the donor-acceptor pair (i.e., there are more donor-acceptor pairs with lower energy), E_{IX} should be larger than the dominant DAP IX peak. Hence, we perform the following procedure to obtain E_{IX}. We first perform a single Gaussian fitting on the IX PL spectrum to get the position of the dominant DAP IX peak. Then we fit the PL spectra with multiple Lorentzians (representing the DAP IX) plus a single Gaussian (representing the band-edge IX), imposing that the Gaussian peak energy must be larger than the dominant DAP IX peak. We take the resulting Gaussian peak energy as E_{IX}. We obtain E_{IX} equal to 1.384 eV, 1.387 eV, and 1.378

eV for dot 1, dot 2, and dot 3 in the main text, respectively. We note that this is the neutral band-edge IX. As described in the main text, from the energy dependence of the lifetime, we found another band-edge IX at lower energy, attributed to the trion peak.

To get the minimum energy of DAP IX (E_0), we consider both the DAP IX linewidth and the band-edge IX. The distance between two adjacent separable Lorentzian peaks should be larger than 60% of their full-width-at-half-maximum (FWHM).). Using this criterion, we obtain $E_0 \leq 1.33\,\text{eV}$. Next, we assume that the difference between E_0 at two different dots should be similar to the difference between the corresponding E_{IX} since, like the E_{IX}, the value of E_0 is also affected by the local strain. We chose the highest E_0 possible for all the dots fulfilling the criteria explained above, obtaining the following E_0: 1.327 eV (dot 1), 1.33 eV (dot 2), and 1.32 (dot 3)).

For determining the peak position of DAP IX, we need to obtain the value of the following parameters beside E_0 (see Eq. (1) in the main text): dielectric constant (ε) and donor-acceptor distance (R_m). We used $\varepsilon = 7.55\varepsilon_0$ based on the MoSe$_2$ and WSe$_2$ out-of-plane dielectric constant[1]. For R_m, since the lattice constant of MoSe$_2$ is approximately the same as WSe$_2$, it can be expressed as

$$R_m = R(m_1, m_2) = \sqrt{\delta^2 + a_0{}^2 \left(m_1{}^2 + m_2{}^2 + m_1 m_2 + m_2 + \frac{1}{3} \right)}, \quad \text{(S1)}$$

where m is the shell number (with R_m is larger for larger value of m), m_1 and m_2 are integers, δ is the interlayer distance, and $a_0 = 0.33\,\text{nm}$ is the lattice constant of MoSe$_2$ (WSe$_2$).

However, Eq. (S1) is only correct if there is no strain variation in the sample, which is not the case for the moiré heterobilayer. For MoSe$_2$/WSe$_2$ heterobilayer, the strain variation (σ_S) can reach $\pm 1.5\%$[2], resulting in the uncertainty in R_m and, thus, in calculated DAP IX peak energy. Based on Eq. (1) in the main text, the uncertainty in DAP IX peak energy due to strain variation can be expressed as

$$\sigma_E = (E - E_0)\left|\sigma_S/(1 + \sigma_S)\right| \approx (E - E_0)\left|\sigma_S\right|, \qquad \text{(S2)}$$

where E is the DAP IX peak energy calculated using Eq. (1) and (S1). From the experimental results, we know that $(E - E_0) \geq 20\,\text{meV}$. Hence, using $\sigma_S = 1\%$, we obtain $\sigma_E \geq 0.2\,\text{meV}$. Considering this σ_E, the predicted DAP IX peaks (red lines in Fig. 2(a-c) in the main text) are taken to be the observed peaks that are within ± 0.2 meV of the calculated DAP IX peaks (using Eq. (1) and (S1)). Similarly, an observed peak matches the DAP IX peaks if its energy is within ± 0.2 meV from the calculated DAP IX peaks.

Section 2. DAP IX energy-lifetime correlation

The fast (k_1) and slow (k_2) decay rates solution for the coupled DAP-band edge IX model (inset of Fig. 3d in the main text) can be expressed as

$$k_1 = \left(\left(k_{DAP} + k_{IX} + 2D \right) + \sqrt{ \left(k_{DAP} - k_{IX} \right)^2 + 4D^2 } \right) \Big/ 2, \quad (S3)$$

$$k_2 = \left(\left(k_{DAP} + k_{IX} + 2D \right) - \sqrt{ \left(k_{DAP} - k_{IX} \right)^2 + 4D^2 } \right) \Big/ 2, \quad (S4)$$

where $k_{DAP} = k_{nr} + k_{r0} \exp\left(-\dfrac{2\alpha}{R_B (E - E_0)} \right)$ is the DAP IX total decay rate with k_{nr} is the

DAP IX nonradiative decay rate, k_{r0} is the DAP IX maximum radiative decay rate,

R_B is the largest Bohr radius between the donor and acceptor, E is the DAP IX

energy, E_0 is the minimum DAP IX energy, and $\alpha = \dfrac{e^2}{4\pi\varepsilon}$ with e is the electron

charge and ε is the effective permittivity, k_{IX} is the band-edge IX decay rate, and D

is the coupling rate between band-edge and DAP IX. While k_{nr} and k_{IX} depends on

the DAP IX energy (see Section S3), it can be assumed to be constant at low power

(as in the case of Fig. 3 in the main text).

The fast and slow decay rates are obtained using Eqs. (S3) and (S4). The maximum

radiative decay rate of DAP IX (k_{r0}) is set to be the same as the maximum radiative

decay rate of exciton in TMD ~ 250 GHz[3]. The energy dependence of D and R_B can

be expressed as

$$D = \sum_i D_{0(i)} \frac{w_{D(i)}^2}{w_{D(i)}^2 + 4\left(E - E_{IX(i)} \right)^2}, \qquad (S5)$$

$$R_B = \sqrt{ R_{B0}^2 + \sum_i A_{R(i)}^2 \frac{w_{R(i)}^2}{w_{R(i)}^2 + 4\left(E - E_{IX(i)} \right)^2} }, \qquad (S6)$$

where E_{IX} is the band-edge IX central energy and the index i is the band-edge IX

index. The values of w_D and w_R (ranging from 2 to 16 meV) are proportional to the

band-edge IX linewidth. When there is no coupling, the Bohr radius is $R_{B0} \sim 0.5$ nm,

comparable to the calculated Bohr radius for some impurity states in monolayer TMD[4]. At maximum coupling, the Bohr radius is increased to ~0.9 nm, which is reasonable given that the radius of the electron (hole) wavefunction in a band-edge IX is ~ 2.4 nm[5].

Section 3. Power dependence of DAP IX lifetime

To capture the power dependence, the following power saturation relations were used:

$$k_{nr}^{DAP(IX)} = k_{nr-max}^{DAP(IX)} \frac{P}{P + P_{sat}^{DAP(IX)}}, \qquad (S7)$$

$$\Delta E_{IX(i)} = \Delta E_{max(i)} \frac{P}{P + P_{sat}^{IX(i)}}, \qquad (S8)$$

where $k_{nr}^{DAP(IX)}$ is the nonradiative rate of the DAP (band-edge) IX, $k_{nr-max}^{DAP(IX)}$ is the maximum nonradiative rate of the DAP (band-edge) IX, $P_{sat}^{DAP(IX)}$ is the saturation power for the DAP (band-edge) IX nonradiative decay, $\Delta E_{max(i)}$ is the (maximum) band-edge IX energy shift, $P_{sat}^{IX(i)}$ is the saturation power for the band-edge IX energy shift, and the index i is the band-edge IX index.

The DAP IX nonradiative recombination is mainly attributed to the Auger process. The power dependence is due to excitation-induced doping. The higher-energy DAP IX has a higher Auger coefficient[6], resulting in the energy-dependent k_{nr-max}^{DAP}. Both the Auger process and exciton-exciton annihilation contribute to the nonradiative rate of band-edge IX. Considering that the band-edge exciton and trion can have different nonradiative rates, the value of k_{nr-max}^{IX} depends on whether the DAP IX is closer to the

16

band-edge exciton or trion. The energy shift of band-edge IX is mainly attributed to the dipole-dipole interaction.

Considering that different processes involved can have different saturation power, we cannot use one value of saturation power for all processes. In the fitting of dot 3 data (Fig. 4 and Extended Data Fig. 8 in the main text), the values of saturation power used are $P_{sat}^{DAP} = 12\,\text{meV}$, $P_{sat}^{IX} = 28\,\text{meV}$, $P_{sat}^{IX(1)} = 6\,\text{meV}$ for exciton, and $P_{sat}^{IX(2)} = 18\,\text{meV}$ for trion. The maximum energy shift is $\Delta E_{\max(i)} \approx 8\,\text{meV}$ for both exciton and trion.

References

1   Laturia, A., Van de Put, M. L. & Vandenberghe, W. G. Dielectric properties of hexagonal boron nitride and transition metal dichalcogenides: from monolayer to bulk. *npj 2D Mater. Appl.* **2**, 6 (2018).

2   Shabani, S. *et al.* Deep moiré potentials in twisted transition metal dichalcogenide bilayers. *Nat. Phys.* **17**, 720-725 (2021).

3   Palummo, M., Bernardi, M. & Grossman, J. C. Exciton radiative lifetimes in two-dimensional transition metal dichalcogenides. *Nano Lett.* **15**, 2794-2800 (2015).

4   Aghajanian, M., Mostofi, A. A. & Lischner, J. Tuning electronic properties of transition-metal dichalcogenides via defect charge. *Sci. Rep.* **8**, 13611 (2018).

5   Karni, O. *et al.* Structure of the moiré exciton captured by imaging its electron and hole. *Nature* **603**, 247-252 (2022).

6   Landsberg, P. T., Adams, M. J. & Fröhlich, H. Theory of donor-acceptor radiative and Auger recombination in simple semiconductors. *Proc. R. Soc. London, Ser. A* **334**, 523-539 (1973).